Cnoidal wave propagation in an elastic metamaterial

Chengyang Mo,[*] Jaspreet Singh,[*] Jordan R. Raney, and Prashant K. Purohit[†]
Department of Mechanical Engineering and Applied Mechanics, University of Pennsylvania, Philadelphia, Pennsylvania 19104, USA

Advances in fabrication techniques have led to a proliferation of studies on new mechanical metamaterials, particularly on elastic and linear phenomena (for example, their phonon spectrum and acoustic band gaps). More recently, there has been a growing interest in nonlinear wave phenomena in these systems, and particularly how geometric parameters affect the propagation of high-amplitude nonlinear waves. In this paper, we analytically, numerically, and experimentally demonstrate the propagation of cnoidal waves in an elastic architected material. This class of traveling waves constitutes a general family of nonlinear waves, which reduce to phonons and solitons under suitable limits. Although cnoidal waves were first discovered as solutions to the conservation laws for shallow water, they have subsequently appeared in contexts as diverse as ion plasmas and nonlinear optics, but have rarely been explored in elastic solids. We show that geometrically nonlinear deformations in architected soft elastic solids can result in cnoidal waves. Insights from our analysis will be critical to controlling the propagation of stress waves in advanced materials.

I. INTRODUCTION

The ubiquity of three-dimensional (3D) printers and the development of novel optimization techniques has allowed researchers to develop mechanical metamaterials that possess unprecedented specific stiffness [1–3], programmable Poisson's ratio [4], damage tolerance [5], multistability [6], etc. This has been achieved by precisely controlling the internal geometric parameters of the metamaterial, leading to nonlinear mechanical behavior. Past work on the propagation of waves in mechanical metamaterials has primarily focused on the propagation of linear waves (or phonons) [7,8], with band gaps often being of chief interest. Recently, additional mechanical systems have been studied for their ability to propagate nonlinear waves, including granular materials relying on Hertzian contact [9,10], tensegrity structures [11], bars and linkages [12], and systems composed of bistable elastic elements [13,14]. Understanding nonlinear wave phenomena in structured media is crucial for controlling stress waves in protective materials, acoustics, vibration mitigation, and aerospace applications [15].

Here we investigate nonlinear oscillatory cnoidal waves, which have received little attention in elastic materials. Cnoidal waves were first described in the late 1800s as periodic solutions of the nonlinear Korteweg–de Vries equation for long waves in shallow water [16]. Since then they have been extensively analyzed in the mathematics and physics communities [17], finding applications in fields as diverse as geophysical fluid dynamics [18], ion plasmas [19], nonlinear optics [20], and geomaterials [21]. Cnoidal waves are related to solitary waves, or solitons, which have been studied extensively in many contexts, including shallow water [22], electrical transmission lines, and lattices of masses and non-

linear springs [23]. In fact, solitons are merely cnoidal waves with infinite period [16]. One instance of an observation of a cnoidal wave in an elastic solid is in the experiments of Nayanov [24] on lithium niobate. Nayanov excited large-amplitude Rayleigh surface waves in a layered sample of lithium niobate and silicon oxide and observed conversion of these waves at high intensities into cnoidal waves and solitons. He showed the characteristic sharp peaks and broad troughs of cnoidal waves even though the input Rayleigh waves were sinusoidal. Apart from this we are not aware of any other observations of cnoidal waves in elastic solids, although they have been mentioned in the theoretical literature on nonlinear waves elsewhere [25,26]. In this paper we develop an analytical, numerical, and experimental framework to show that an elastic metamaterial (Fig. 1) can support cnoidal waves as a more general periodic nonlinear propagating wave, which include the previously observed soliton solutions [27] as one limit. Moreover, the nonlinearities in our mechanical metamaterials can be tailored over a wide range since they are made of 3D-printed soft elastomers whose geometry can be controlled.

II. THEORY

Our medium for wave propagation is a 3D-printed network of N columns (of six) of rotationally offset squares, composed of polydimethylsiloxane (PDMS) and each with a copper cylinder in the center as shown in Fig. 1(a). Each (jth) column of squares is capable of translation u_j and rotation θ_j. The squares have a diagonal length of $2l \approx 11.3$ mm and are rotated by $\theta_0 = 25°$ from the y axis. The PDMS network exerts both forces and torques on the four corners of the square with a linear spring (with stretch stiffness k) and a torsional spring (with twist stiffness k_θ), respectively. By assuming periodic boundary conditions in the y direction, the force and torque balance for each square of mass m and moment of inertia J in terms of nondimensional displacement $U_j = u_j/2l \cos\theta_0$ and rotation θ_j are (the material constants are taken directly from

---

[*]These authors contributed equally to this paper.
[†]Corresponding author: purohit@seas.upenn.edu

Deng *et al.* [27] since we use a similar specimen)

$$\frac{\partial^2 U_j}{\partial T^2} = U_{j+1} - 2U_j + U_{j-1} - \frac{1}{2l\cos\theta_0}\{\cos(\theta_{j+1}+\theta_0) - \cos[\theta_{j-1}+\theta_0+K(\theta_{j+1}-\theta_{j-1})\sin(\theta_j+\theta_0)]\},$$

$$\frac{\partial^2 \theta_j}{\partial T^2} = \alpha^2\{-K(\theta_{j+1}+6\theta_j+\theta_{j-1}) - 2(U_{j+1}-U_{j-1})\cos\theta_0\sin(\theta_j+\theta_0) + \sin(\theta_j+\theta_0)[\cos(\theta_{j+1}+\theta_0)+6\cos(\theta_j+\theta_0)$$

$$+ \cos(\theta_{j-1}+\theta_0) - 8\cos\theta_0] + \cos(\theta_j+\theta_0)[\sin(\theta_{j+1}+\theta_0) - 2\sin(\theta_j+\theta_0) + \sin(\theta_{j-1}+\theta_0)]\}, \quad (1)$$

where $U_j = U_j(t)$, $\theta_j = \theta_j(t)$, $T = t\sqrt{k/m}$, $\alpha = l\sqrt{m/J}$, and $K = k_\theta/kl^2$.

The discrete set of $2N$-equations can be condensed into two *continuum* equations by restricting rotation to small angles such that $\sin\theta_j \approx \theta_j$ and $\cos\theta_j = 1$, and introducing dimensionless length coordinate X and dimensionless time T such that $\partial U/\partial X = \frac{1}{2}(U_{j+1}-U_{j-1})$, $\partial^2 U/\partial X^2 = U_{j+1} - 2U_j + U_{j-1}$, $\partial\theta/\partial X = \frac{1}{2}(\theta_{j+1}-\theta_{j-1})$, and $\partial^2\theta/\partial X^2 = \theta_{j+1} - 2\theta_j + \theta_{j-1}$. Performing the calculations [27] yields the following equations for $U(\zeta)$ and $\theta(\zeta)$:

$$\frac{d^2\theta}{d\zeta^2} + P\theta + Q\theta^2 = 0, \quad (2a)$$

$$\frac{dU}{d\zeta} = -\frac{(1-K)\tan\theta_0}{1-c^2}\theta, \quad (2b)$$

where $\zeta = X - cT$ is the *traveling wave coordinate*, and c is the normalized wave speed. P and Q are constants that depend on the stiffness parameters that can be calculated from geometry and material parameters:

$$P = \frac{4\alpha^2\beta}{1-c^2}[(2c^2-1-K)\sin^2\theta_0 - 2(1-c^2)K],$$

$$Q = \frac{2\alpha^2\beta}{1-c^2}[(2c^2-1-K)\sin\theta_0], \quad (3)$$

where $\beta = 1/[\alpha^2(\cos 2\theta_0 - K) - c^2]$. Consider a solution Eq. (2a) in the following form, called the cnoidal wave solution:

$$\theta(\zeta) = A\,\mathrm{cn}^2\left(\frac{\zeta}{W}|\kappa^2\right) + B, \quad 0 \leqslant \kappa^2 \leqslant 1, \quad (4)$$

where $\mathrm{cn}(\frac{\zeta}{W}|\kappa^2)$ is a Jacobi elliptic function [28]. When the elliptic modulus $\kappa^2 \to 1$, we recover the soliton solution [27]:

$$\lim_{\kappa^2 \to 1}\theta(\zeta) = A\,\mathrm{sech}^2\left(\frac{\zeta}{W}\right). \quad (5)$$

Moreover, when $\kappa^2 \to 0$, $\theta(\zeta)$ behaves like a sinusoid:

$$\lim_{\kappa^2 \to 0}\theta(\zeta) = -\frac{A}{2}\cos(\sqrt{P}\zeta). \quad (6)$$

Thus, our proposed cnoidal wave solution [Eq. (4)] spans the entire range from phonons (linear waves) to solitons. For $0 < \kappa^2 < 1$, by plugging the proposed solution Eq. (4) back into Eq. (2a) and setting all coefficients of $\mathrm{cn}^n(\frac{\zeta}{W}|\kappa^2)$ to zero, we can obtain the following solution:

$$A = \frac{3|P|}{2Q}\frac{\kappa^2}{\sqrt{\kappa^4-\kappa^2+1}},$$

$$B = -\frac{1}{2Q}\left[P - |P|\frac{2\kappa^2-1}{\sqrt{\kappa^4-\kappa^2+1}}\right],$$

$$W = \frac{2}{\sqrt{|P|}}(\kappa^4-\kappa^2+1)^{\frac{1}{4}}. \quad (7)$$

Note that our solution [Eq. (4)] is not sinusoidal but is periodic with a period $4\mathbf{K}(\kappa^2)$, where $\mathbf{K}(\kappa^2)$ is the complete elliptic integral of the first kind [28]. However, Eq. (7) cannot fully describe the solution, since P and Q are functions of the wave
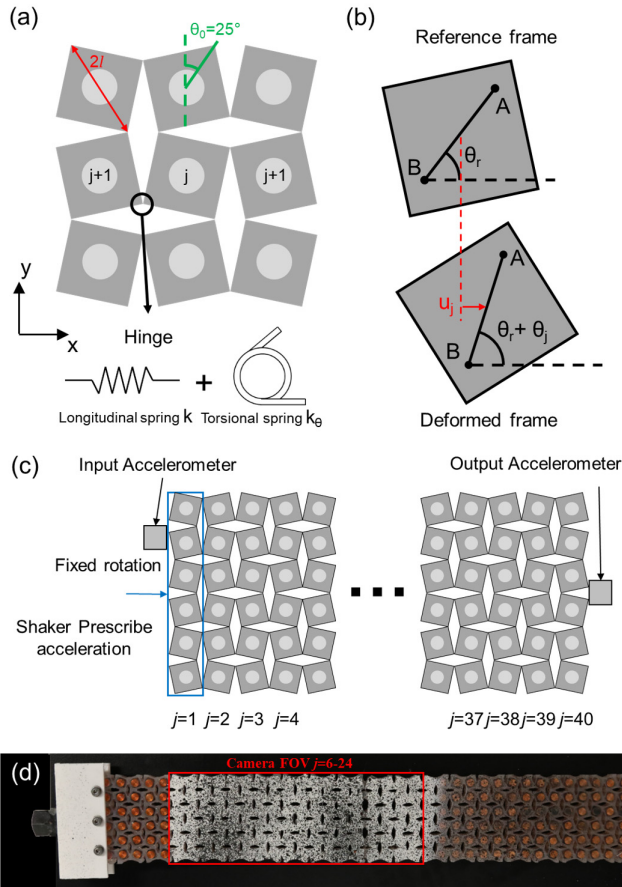

FIG. 1. (a) Schematic of the system and geometry of the squares. (b) Displacement and rotation of each square. (c) Experimental setup including a shaker that provides the cnoidal wave input and accelerometers at both ends that measure the input and output acceleration. (d) Image of the entire sample, with the portion recorded via a high-speed camera indicated by the red rectangle.
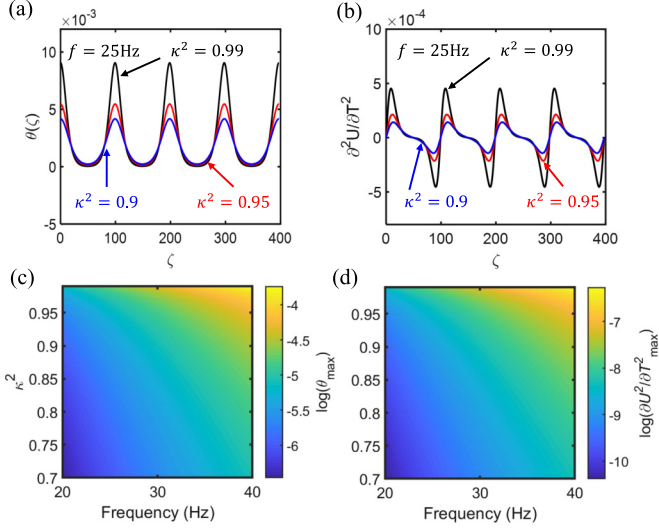
FIG. 2. Analytical cnoidal wave solutions for $f = 25\,\mathrm{Hz}$ and $\kappa^2 = 0.99$, 0.95, and 0.90: (a) $\theta(\zeta) = A\mathrm{cn}^2(\frac{\zeta}{W}|\kappa^2) + B$ [Eq. (4)]; (b) $\partial^2 U/\partial T^2(\zeta)$ [Eq. (9)]; (c, d) amplitude of θ and $\partial^2 U/\partial T^2$ solution vs f and κ^2.

speed c. Another parameter other than the elliptic modulus κ^2 is needed to completely describe our solution. An experimentally convenient choice is frequency $f = \frac{v}{w}$, where v is the dimensional wave speed and w is the dimensional wavelength. By applying the dimensional constants the frequency can be expressed with two other unknowns (W and c) as

$$f = \frac{c}{2\mathbf{K}W\sqrt{m/k}}. \tag{8}$$

The four unknowns of the problem A, B, W, and c can be solved via four nonlinear equations [Eq. (7) and Eq. (8)]. After fully characterizing θ, the other coupled variable displacement $U(\zeta)$ can be solved by substituting Eq. (4) in Eq. (2b). The acceleration $\partial^2 U/\partial T^2$ can also be calculated:

$$U(\zeta) = \frac{(K-1)\tan\theta_0}{1-c^2}\int_0^\zeta \left[A\mathrm{cn}^2\left(\frac{y}{W}|\kappa\right) + B\right]dy,$$

$$\frac{\partial^2 U}{\partial T^2} = \frac{2Ac^2(1-K)}{W(1-c^2)}\tan\theta_0\, \mathrm{cn}\left(\frac{\zeta}{W}|\kappa^2\right)\mathrm{sn}\left(\frac{\zeta}{W}|\kappa^2\right)$$

$$\times\,\mathrm{dn}\left(\frac{\zeta}{W}|\kappa^2\right). \tag{9}$$

We compute the wave speed c within an experimentally accessible range of parameters: $20\,\mathrm{Hz} < f < 40\,\mathrm{Hz}$, and $0.7 < \kappa^2 < 0.99$. In this range, the wave speed $c \approx 0.82$ (similar to the speed found for solitons previously) is insensitive to the variations in parameters. Figures 2(a) and 2(b) show the cnoidal solution in rotation θ and acceleration $\partial^2 U/\partial T^2$ for $f = 25\,\mathrm{Hz}$. Note that the curves are periodic but not sinusoidal. We examine the dependence of the amplitude of the cnoidal wave [Eq. (4)] on frequency f and elliptic modulus κ^2 by plotting it on a two-dimensional f-κ^2 plane. Figure 2(c) shows that for a fixed frequency, the rotation amplitude increases with elliptic modulus, and for a fixed elliptic modulus the amplitude increases with frequency. Similar trends are observed in the acceleration amplitude, shown in Fig. 2(d).

We also explored the effect of geometry and the material constants of the system on the solution shown here (details are found in the Supplemental Material [29] Figs. S2 and S3). Specifically, the wave speed of the cnoidal wave solution increases monotonically with decreasing θ_0 and increasing K. The amplitude (A) and offset (B) have local minima and maxima as a function of θ but change monotonically as a function of K.

The governing equation [Eq. (2)] is a nonlinear differential equation whose solutions may not be unique. While Eq. (4) is one solution that satisfies the equations, another oscillatory traveling wave solution to Eq. (2) is

$$\theta(\zeta) = \frac{A}{\mathrm{dn}^2\left(\frac{\zeta}{W}|\kappa^2\right)} + B, \tag{10}$$

where $\mathrm{dn}(\frac{\zeta}{W}|\kappa^2)$ is another Jacobi elliptic function [28]. The displacement and acceleration for this solution can also be computed as

$$U(\zeta) = \frac{(K-1)\tan\theta_0}{1-c^2}\int_0^\zeta \left[\frac{A}{\mathrm{dn}^2\left(\frac{y}{W}|\kappa\right)} + B\right]dy,$$

$$\frac{\partial^2 U}{\partial T^2} = c^2\frac{(K-1)\tan\theta_0}{1-c^2}\frac{2A\kappa^2}{W}\frac{\mathrm{cn}\left(\frac{\zeta}{W}|\kappa^2\right)\mathrm{sn}\left(\frac{\zeta}{W}|\kappa^2\right)}{\mathrm{dn}^3\left(\frac{\zeta}{W}|\kappa^2\right)}. \tag{11}$$

Here, too, the values of A, B, and W depend on the elliptic modulus κ^2, and the parameters P and Q are

$$A = \frac{3|P|}{2Q}\frac{\kappa^2 - 1}{\sqrt{\kappa^4 - \kappa^2 + 1}},$$

$$B = -\frac{1}{2Q}\left(P + |P|\frac{2 - \kappa^2}{\sqrt{\kappa^4 - \kappa^2 + 1}}\right),$$

$$W = \frac{2}{\sqrt{|P|}(\kappa^4 - \kappa^2 + 1)^{\frac{1}{4}}}. \tag{12}$$

As $\kappa^2 \to 1$ we see that $A \to 0$, suggesting that, unlike Eq. (4), this solution does not reduce to a soliton in that limit. Also, as $\kappa^2 \to 0$, the elliptic function $\mathrm{dn}(x|k) \to 1$, which is not sinusoidal. Hence, this solution is distinct from the cnoidal wave solution even though both are nonlinear oscillatory traveling waves. For the rest of the paper we focus exclusively on the solution provided by Eq. (4).

III. NUMERICS

Next, we validate our traveling wave solutions obtained in Eq. (4). To do this, we numerically solve the *ab initio* force and torque balance equations [Eq. (1)] for each individual square. For a sample consisting of N squares, we have $2N$ second-order coupled ordinary differential equations in displacement $U_j(T)$, and rotation $\theta_j(T)$ for the jth square. The first ($j = 1$) square in the sample is externally excited using a shaker, hence the boundary condition is

$$U_1(T) = U(\zeta)|_{X=0}, \quad \theta_1(T) = 0, \tag{13}$$

where $U(\zeta)$ is given by Eq. (9). We use a zero force and torque boundary condition for the $j = N$ square. We solve this system of ODEs numerically in MATLAB for a long sample
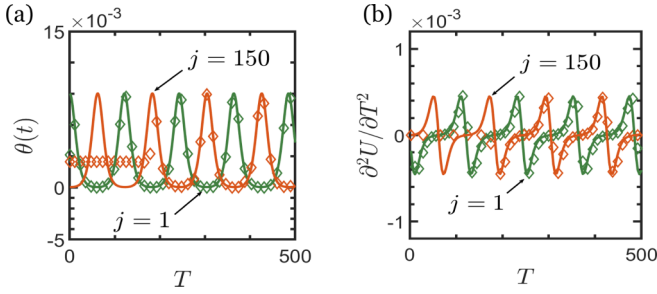
FIG. 3. Comparison between the numerical results (diamonds) obtained by solving the $2N$ discrete differential equations [Eq. (1)] and the analytical (solid lines) results [Eqs. (4) and (9)]: (a) θ and (b) $\partial^2 U/\partial T^2$ for $f = 25$ Hz and $\kappa^2 = 0.90$.

($N = 1000$) to test our analytical traveling wave solutions in Eq. (4). We plot the theoretical [Eq. (4)] and numerical results for rotation θ and acceleration $\partial^2 U/\partial T^2$ in Fig. 3. Figure 3(a) shows the results for $\theta_j(t)$ for $j = 1$ and $j = 150$ when the specimen is excited using a displacement waveform in Eq. (9) for $\kappa^2 = 0.90$, and Fig. 3(b) shows the corresponding acceleration plots. We indeed observe that the excitation given to the $j = 1$ square [Eq. (13)] propagates in a self-similar manner for both the rotation and acceleration. Agreement between our analytical result and numerical simulations validates the cnoidal wave solution provided. [See Fig. S7 in the Supplemental Material [29] for validation of Eq. (10).]

IV. EXPERIMENTS

Next, we conduct experiments to observe the propagation of the cnoidal wave in a specimen consisting of $N = 40$ columns of squares. One end of the specimen is attached to a shaker (APS 113) which provides periodic motion to the $j = 1$ column. The motion of the shaker is controlled by a function generator (FeelTech FY2300a) via an amplifier (APS 125), which allows us to feed a cnoidal waveform [i.e., Fig. 2(b)] to our system. We measure the acceleration at the input ($j = 1$) and the output ($j = 40$) by attaching piezoelectric accelerometers (PCB 352A24) at both ends [see Fig. 1(c)]. Additionally, we record the experiment using a high-speed camera (Photron Mini AX-200) operating at 6400 frames per second [see Fig. 1(d)] to measure the rotation θ_j. A speckle pattern is applied on the specimen in order to provide sufficient contrast for digital image correlation (DIC) analysis, performed using commercially available software (GOM Correlate). [Note also that we applied DIC only in the region marked by the red rectangle in Fig. 1(d), due to the limits of field of view of our camera.] The rotation of each square is obtained continuously by tracking two points within each square. As shown in Fig. 1(b), the initial vector $\overrightarrow{AB}$ forms an angle θ_r with the x axis in the reference frame. At a later time t, the deformed vector $\overrightarrow{A'B'}$ forms a new angle $\theta_r + \theta_j$, with θ_j denoting the rotation of the square j at time t. For each combination of frequency f and κ^2, the current supplied to the shaker is calibrated before each test (details are found in the Supplemental Material [29]). The specimen is excited for 10 s to ensure stable propagation, during which the accelerometers continuously record acceleration. The high-
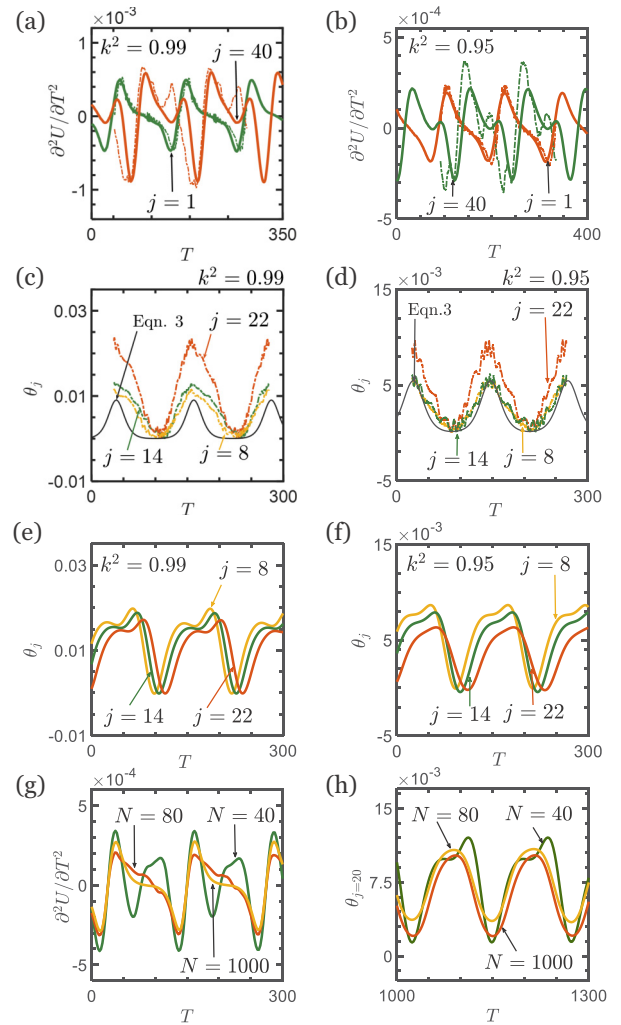

FIG. 4. The comparison between experimental (dash lines) and numerical results (solid lines) of $\partial^2 U/\partial T^2$ data for $f = 25$ Hz and $\kappa^2 = $ (a) 0.99 and (b) 0.95. Experimental result of θ (dash lines) compared to analytical solution (solid line) for $f = 25$ Hz and $\kappa^2 = $ (c) 0.99 and (d) 0.95. Numerical result of θ for $f = 25$ Hz and $\kappa^2 = $ (e) 0.99 and (f) 0.95. Numerical result of systems with various sample length (N) for $\kappa^2 = 0.95$: (g) $\partial^2 U/\partial T^2$ and (h) $\theta_{j=20}$.

speed camera records for 3 s in the middle of this interval of excitation (for tracking rotations θ_j).

We excite the sample (at $j = 1$) with the cnoidal wave form at $f = 25$ Hz for two values of elliptic modulus, $\kappa^2 = 0.99$ and 0.95. With these values the shaker provides sufficient amplitude [Eq. (7)] to allow U_j and θ_j to be measured with the high-speed camera. The acceleration at both the input ($j = 1$) and output ($j = 40$) squares are also collected [see representative data in Figs. 4(a) and 4(b)]. The cnoidal wave propagates through our system while preserving its amplitude and its shape. The experimental wave speed can be calculated from the peak offset time of the measured acceleration waves. For $\kappa^2 = 0.99$, the experimental wave speed is $c = 0.821$ (see details in the Supplemental Material [29]), which is in excellent agreement with the analytical prediction ($c = 0.8184$). For $\kappa^2 = 0.95$, the experimental wave speed is $c = 0.8804$, while the analytical prediction is $c = 0.8187$. The difference

between the analytical solution and measurement is slightly larger in this case because the amplitudes of θ_j and the acceleration are much smaller, leading to larger experimental uncertainty.

The rotations of the three representative squares within the field of view during wave propagation for $\kappa^2 = 0.99$ and 0.95 are presented in Figs. 4(c) and 4(d), respectively. Since the analytical form of the cnoidal wave is found in the rotation, measuring the angle of rotation provides the most direct evidence that the wave propagating through our system is indeed a cnoidal wave. For $\kappa^2 = 0.99$ [Fig. 4(c)], the amplitude of rotation is in close agreement with the expectations from the cnoidal wave solution. The shape does not exactly match the analytical solution, though it is periodic but not sinusoidal, most clearly for $\theta_{j=8}$. A closer match in both shape and amplitude is obtained for $\kappa^2 = 0.95$ [Fig. 4(d)].

Though we observe good overall agreement between the experiments and analytical predictions, two discrepancies are immediately apparent: First, the output accelerometer shows an additional peak during the experiments which is not expected from the analytical solution. Second, $\theta_{j=22}$ has a significantly larger amplitude than $\theta_{j=8}$ and $\theta_{j=14}$. Both of these can be explained with the help of the numerical simulations.

To understand the additional peak in the accelerometer data, we numerically solve the *ab initio* force and torque balance equations [Eq. (1)]. We use the same boundary conditions, but now we solve the equations with only $N = 40$ instead of $N = 1000$, in order to account for finite size effects [Figs. 4(a) and 4(b)]. The acceleration of the terminal squares ($j = 40$) matches well with the experimental results in amplitude and shows the same anomalous peak observed in experiments. Rotations are also obtained from the numerical results and reported in Figs. 4(e) and 4(f). Here, too, we observe a second peak in each period of the numerical traveling wave solution, which disappears as the length of the specimen increases (the DIC measurements were unable to capture the anomalous peak in θ, probably due to the resolution limit of the rotation measurements, i.e., ~ 0.003 rad). Next, we obtain numerical results for additional specimens with various lengths ($N = 80$ and $N = 1000$ squares), plotted in Figs. 4(g) and 4(h). We find that as we increase the length of the specimen, the magnitude of the secondary peak decreases in both acceleration and rotation. Hence, we conclude that the second peak in the experiment indeed arises from boundary effects due to the finite specimen size.

Regarding the anomalous amplitude of $\theta_{j=22}$, this appears to result from fabrication defects in the specimen. The spec-

imen was fabricated in two parts (squares $j = 1$–20 were fabricated together, and squares $j = 21$–40 were fabricated together), and subsequently joined via additional PDMS. We observe that the second half of the specimen is slightly thicker by $\sim 10\%$ than the first half, effectively increasing the in-plane stiffness and allowing larger-than-expected amplitudes to occur in the second half, particularly near the boundary. Interestingly, we observe that the cnoidal wave propagates unhindered through this boundary, maintaining its shape, but just altering in amplitude [see the Supplemental Material [29] for a numerical solution to Eq. (1)]. These effects could be easily harnessed using our 3D-printing methods to intentionally customize the wave propagation depending on the needs of a given application.

V. CONCLUSION

In this paper, we have shown analytically, numerically, and experimentally that nonlinear cnoidal waves can propagate in a purely elastic metamaterial composed of a network of rotationally offset squares. Our analytical solutions uncover a whole class of oscillatory traveling waves in solids that span from linear sinusoidal waves to vector solitons. To experimentally characterize these we use a high-speed camera in combination with accelerometers to monitor both the translational motion and the rotation of the squares. Our numerical simulations show that the minor discrepancies between the experiments and the analytical solution are artifacts of the limited sample length. The discovery of this oscillatory traveling wave is a crucial step toward understanding the propagation of nonlinear waves in structured media. This is important for applications in protective materials, acoustics, vibration mitigation, and aerospace and could potentially lead to more exotic dynamic properties, such as the transmission of information encoded in the frequency and shape of such waves in elastic metamaterials. The 3D printability of our metamaterial also allows unique control of the amplitude and shape of cnoidal waves propagating through the system.

ACKNOWLEDGMENTS

[1] T. A. Schaedler, A. J. Jacobsen, A. Torrents, A. E. Sorensen, J. Lian, J. R. Greer, L. Valdevit, and W. B. Carter, Ultralight metallic microlattices, Science **334**, 962 (2011).

[2] L. R. Meza, S. Das, and J. R. Greer, Strong, lightweight, and recoverable three-dimensional ceramic nanolattices, Science **345**, 1322 (2014).

[3] X. Zheng, H. Lee, T. H. Weisgraber, M. Shusteff, J. DeOtte, E. B. Duoss, J. D. Kuntz, M. M. Biener, Q. Ge, J. A. Jackson,

S. O. Kucheyev, N. X. Fang, and C. M. Spadaccini, Ultralight, ultrastiff mechanical metamaterials, Science **344**, 1373 (2014).

[4] A. Clausen, F. Wang, J. S. Jensen, O. Sigmund, and J. A. Lewis, Topology optimized architectures with programmable Poisson's ratio over large deformations, Adv. Mater. **27**, 5523 (2015).

[5] M.-S. Pham, C. Liu, I. Todd, and J. Lertthanasarn, Damage-tolerant architected materials inspired by crystal microstructure, Nature (London) **565**, 305 (2019).

[6] S. Shan, S. H. Kang, J. R. Raney, P. Wang, L. Fang, F. Candido, J. A. Lewis, and K. Bertoldi, Multistable architected materials for trapping elastic strain energy, Adv. Mater. **27**, 4296 (2015).

[7] V. Kunin, S. Yang, Y. Cho, P. Deymier, and D. J. Srolovitz, Static and dynamic elastic properties of fractal-cut materials, Extreme Mech. Lett. **6**, 103 (2016).

[8] A. J. Zelhofer and D. M. Kochmann, On acoustic wave beaming in two-dimensional structural lattices, Int. J. Solids Struct. **115**, 248 (2017).

[9] V. F. Nesterenko, Propagation of nonlinear compression pulses in granular media, J. Appl. Mech. Tech. Phys. **24**, 733 (1983).

[10] A. Spadoni and C. Daraio, Generation and control of sound bullets with a nonlinear acoustic lens, Proc. Natl. Acad. Sci. USA **107**, 7230 (2010).

[11] F. Fraternali, L. Senatore, and C. Daraio, Solitary waves on tensegrity lattices, J. Mech. Phys. Solids **60**, 1137 (2012).

[12] B. G. Chen, N. Upadhyaya, and V. Vitelli, Nonlinear conduction via solitons in a topological mechanical insulator, Proc. Natl. Acad. Sci. USA **111**, 13004 (2014).

[13] N. Nadkarni, C. Daraio, and D. M. Kochmann, Dynamics of periodic mechanical structures containing bistable elastic elements: From elastic to solitary wave propagation, Phys. Rev. E **90**, 023204 (2014).

[14] J. R. Raney, N. Nadkarni, C. Daraio, D. M. Kochmann, J. A. Lewis, and K. Bertoldi, Stable propagation of mechanical signals in soft media using stored elastic energy, Proc. Natl. Acad. Sci. USA **113**, 9722 (2016).

[15] M. A. Porter, P. G. Kevrekidis, and C. Daraio, Granular crystals: Nonlinear dynamics meets materials engineering, Phys. Today **68**, 44 (2015).

[16] G. B. Whitham, *Linear and Nonlinear Waves* (John Wiley, New York, 1999).

[17] J. P. Boyd, The double cnoidal wave of the Korteweg–de Vries equation: An overview, J. Math. Phys. **25**, 3390 (1984).

[18] R. A. Clarke, Solitary and cnoidal planetary waves, Geophys. Astrophys. Fluid Dyn. **2**, 343 (1971).

[19] R. E. Tolba, W. M. Moslem, A. A. Elsadany, N. A. El-Bedwehy, and S. K. El-Labany, Development of cnoidal waves in positively charged dusty plasmas, IEEE Trans. Plasma Sci. **45**, 2552 (2017).

[20] M. Wilson, V. Aboites, A. N Pisarchik, F. Ruiz-Oliveras, and M. Taki, Stable cnoidal wave formation in an erbium-doped fiber laser, Appl. Phys. Express **4**, 112701 (2011).

[21] E. Veveakis and K. Regenauer-Lieb, Cnoidal waves in solids, J. Mech. Phys. Solids **78**, 231 (2015).

[22] M. Hayatdavoodi, B. Seiffert, and R. C. Ertekin, Experiments and calculations of cnoidal wave loads on a flat plate in shallow-water, J. Ocean Eng. Marine Energy **1**, 77 (2015).

[23] M. Remoissenet, *Waves Called Solitons* (Springer-Verlag, Berlin, 1999).

[24] V. I. Nayanov, Surface acoustic cnoidal waves and solitons in a LiNbO$_3$-(SiO film) structure, JETP Lett. **44**, 314 (1986).

[25] A. M. Samsonov, *Strain Solitons in Solids and How to Construct Them* (Chapman and Hall/CRC, Boca Raton, FL, 2001).

[26] A. M. Samsonov, Nonlinear Strain Waves in Elastic Waveguides, in *Nonlinear Waves in Solids*, edited by A. Jeffrey and J. Engelbrecht (Springer, Vienna, 1994), pp. 349–382.

[27] B. Deng, J. R. Raney, V. Tournat, and K. Bertoldi, Elastic Vector Solitons in Soft Architected Materials, Phys. Rev. Lett. **118**, 204102 (2017).

[28] M. Abramowitz and I. A. Stegun, *Handbook of Mathematical Functions with Formulas, Graphs, and Mathematical Tables* (U.S. Government Printing Office, Washington, DC, 1972).

[29] See Supplemental Material at http://link.aps.org/supplemental/10.1103/PhysRevE.100.013001 for detailed theoretical derivations, experimental setup, and additional numerical results.